PET-based dose delivery verification in proton therapy: a GATE based simulation study of five PET system designs in clinical conditions

2013 Phys. Med. Biol. 58 6867

(http://iopscience.iop.org/0031-9155/58/19/6867)

IOP Publishing Physics in Medicine and Biology

Phys. Med. Biol. **58** (2013) 6867–6885 doi:10.1088/0031-9155/58/19/6867

PET-based dose delivery verification in proton therapy: a GATE based simulation study of five PET system designs in clinical conditions

Charlotte Robert[1], Nicolas Fourrier[1], David Sarrut[2,3], Simon Stute[4], Pierre Gueth[2], Loïc Grevillot[2] and Irène Buvat[1]

[1] IMNC–UMR 8165 CNRS, Universités Paris 7 et Paris 11, Bât 440, F-91406 Orsay, France
[2] CREATIS–UMR 5220 CNRS, Université de Lyon, F-69622 Villeurbanne, France
[3] Léon Bérard cancer center, Université de Lyon, France
[4] CEA, Service Hospitalier Frédéric Joliot, F-91401 Orsay, France

E-mail: robert@imnc.in2p3.fr

Received 26 March 2013, in final form 16 August 2013
Published 12 September 2013
Online at stacks.iop.org/PMB/58/6867

Abstract

PET is a promising technique for *in vivo* treatment verification in hadrontherapy. Three main PET geometries dedicated to in-beam treatment monitoring have been proposed in the literature: the dual-head PET geometry, the OpenPET geometry and the slanted-closed ring geometry. The aim of this work is to characterize the performance of two of these dedicated PET detectors in realistic clinical conditions. Several configurations of the dual-head PET and OpenPET systems were simulated using GATE v6.2. For the dual-head configuration, two aperture angles (15° and 45°) were studied. For the OpenPET system, two gaps between rings were investigated (110 and 160 mm). A full-ring PET system was also simulated as a reference. After preliminary evaluation of the sensitivity and spatial resolution using a Derenzo phantom, a real small-field head and neck treatment plan was simulated, with and without introducing patient displacements. No wash-out was taken into account. 3D maps of the annihilation photon locations were deduced from the PET data acquired right after the treatment session (5 min acquisition) using a dedicated OS-EM reconstruction algorithm. Detection sensitivity at the center of the field-of-view (FOV) varied from 5.2% (45° dual-head system) to 7.0% (full-ring PET). The dual-head systems had a more uniform efficiency within the FOV than the OpenPET systems. The spatial resolution strongly depended on the location within the FOV for the $\phi = 45°$ dual-head system and for the two OpenPET systems. All investigated architectures identified the magnitude of mispositioning introduced in the simulations within a 1.5 mm accuracy. The variability on the estimated mispositionings was less than 2 mm for all PET systems.

(Some figures may appear in colour only in the online journal)

1. Introduction

PET imaging has been demonstrated to be a promising method for *in vivo* dose deposition monitoring in hadrontherapy (eg, Parodi *et al* 2002, Parodi *et al* 2007a). The method involves comparison of the expected map of the annihilation photons created by β^+-emitters resulting from nuclear fragmentation induced by the irradiation with the measured PET images. Expected maps are calculated from the treatment plan using Monte Carlo simulations. Geant4 (Agostinelli *et al* 2003) and FLUKA (Battistoni *et al* 2007) are the two codes most used in this field. They have been previously validated by several studies (Parodi *et al* 2002, Pshenichnov *et al* 2006, Sommerer *et al* 2006, 2009, Seravalli *et al* 2012, Titt *et al* 2012, Robert *et al* 2013). In hadrontherapy, a high precision in the treatment delivery is crucial to make the most of the ballistics of hadrons, i.e. to safely reduce security margins while sparing healthy tissues. PET imaging can be used to detect inaccuracies in the patient positioning as well as anatomical modifications that can occur between the time the treatment plan is established and the treatment session itself.

Three approaches of PET-based dose delivery verification have been investigated: in-beam PET (Llacer 1988), in-room PET (Zhu *et al* 2011) and offline PET (Parodi *et al* 2007a, 2007b). A detailed review on these different methods can be found in Shakirin *et al* (2011). The present study is dedicated to the characterization of the performance of two in-beam PET systems in realistic clinical conditions: the dual-head PET system and the OpenPET systems.

In-beam PET was proposed and used for the first time in Berkeley (Llacer 1988). The method was applied in clinical routine from 1997 to 2008 at the GSI facility, Darmstadt, Germany (Pawelke *et al* 1997, Enghardt *et al* 1999). In-beam PET systems are installed in the treatment room, directly around the patient (Pawelke *et al* 1997, Iseki *et al* 2003, Nishio *et al* 2010). These systems have dedicated geometries so that the detectors do not interfere with the beam path. Three main geometries have been proposed so far: a dual-head PET system (Enghardt *et al* 1999), a so-called OpenPET system (Yamaya *et al* 2008) and a slanted closed-ring tomograph (Crespo *et al* 2007, Tashima *et al* 2012). Compared to the other two configurations, dual-head PET systems offer more degrees of freedom for patient positioning.

For all systems, only coincidences detected during the pauses of the pulsed treatment beam or directly after the irradiation are used for image reconstruction in order to avoid contamination by prompt secondary radiations (prompt gammas and neutrons). These acquisition schemes require a precise synchronization with the beam control system, which is not feasible in all facilities (new facilities with continuous cyclotron beam irradiation for instance). Nevertheless, the in-beam PET method has two main advantages: first, short-lived radionuclides such as ^{10}C ($T_{1/2} = 19.3$ s) and ^{15}O ($T_{1/2} = 2.03$ min) can be detected; second, only a negligible biological wash-out affects the measured activity distributions (Fiedler *et al* 2008).

Dual-head architectures are characterized by two opposite detection heads (figure 1). The first prototype, beta activity measurements at the therapy with energetic ions, was used from 1997 to 2008 to monitor pilot carbon-ion irradiations at GSI. Each head had a 42×21 cm^2 area, resulting in an approximate 9% geometrical detection efficiency at the center of the tomograph. BGO detectors were used. A complete description of this system can be found in Enghardt *et al* (1999) and Enghardt *et al* (2004). Three studies were dedicated to the optimization of this architecture. In Crespo *et al* (2006), the influence of the opening angle ϕ (figure 1) on the detection efficiency and reconstruction artifacts was analyzed. A fully 3D, rebinning-free, maximum likelihood expectation maximization algorithm, applicable to full-ring and dual-head tomographs, was developed. Results show that gaps $\phi = 46^\circ$ were optimal for in-beam PET imaging and did not lead to significant image deterioration. In this study, realistic treatment plans corresponding to head and neck and pelvis carbon-ion

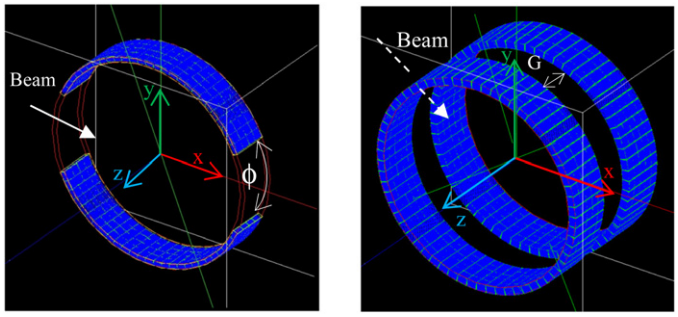

Figure 1. Simulation of the dual-head system (left) and OpenPET system (right) in GATE. Dual-head systems are characterized by the opening angle ϕ and OpenPET systems by the gap G between the detector rings. z corresponds to the axial direction of the PET systems and x and y are the transaxial directions.

irradiations were also simulated. β^+-activity distributions were obtained using the PosGen Monte Carlo code (Pönisch *et al* 2004). Simulated statistics were multiplied by a factor 10 to compare reconstructed images provided by the different detector geometries without being influenced by the low statistics. No detector electronics was modeled. In Crespo *et al* (2007), a new reconstruction algorithm accounting for the time-of-flight information was developed. The study shows that for coincidence time resolution $\leqslant$200 ps, reconstruction artifacts were significantly reduced for $\phi = 46^\circ$ opening angles. A comparable simulation-based study was carried out by Surti *et al* (2011) for proton beam therapy. In this work, β^+-activity distributions were obtained using Geant4 and the EGS4 simulation tool was used to simulate PET systems (Adam *et al* 1999, Surti *et al* 2004). Water-filled cylinders were irradiated. No realistic treatment plans were modeled.

More recently, the OpenPET geometry was proposed by Yamaya *et al* (2008). It consists in two axially separated detector rings (figure 1). In Yamaya *et al* (2008), the OpenPET geometry was characterized in terms of sensitivity, spatial resolution and reconstruction artifacts. Reconstructed images of a hollow sphere phantom were also compared to reconstructed images obtained with a $\phi = 45^\circ$ dual-head system. This study concluded that the gap between the two rings should not exceed the axial length of one ring to avoid reconstruction artifacts. In this work, no details were given about the simulation tool. No realistic treatment plan was implemented. Experimental results obtained with a small OpenPET prototype can be found in Yamaya *et al* (2008) and Yoshida *et al* (2012). Alternative OpenPET architectures, which improve the uniformity of the sensitivity while keeping a gap for the beam path, are described in Yamaya *et al* (2008) and Yamaya *et al* (2009). In Tashima *et al* (2012), a second-generation elliptical OpenPET geometry was investigated.

In this study, several dual-head PET and OpenPET systems were simulated using the GATE Monte Carlo simulation tool (Jan *et al* 2004, 2011). The architectures were compared in terms of sensitivity and spatial resolution by setting identical simulation parameters including realistic modeling of the detector electronics. Clinical β^+-emitter distributions corresponding to a head and neck treatment plan were also simulated. They were used as inputs of imaging acquisitions corresponding to each dedicated PET system to determine the ability of each system to correctly detect mispositionings of the patient. The simulated scenario corresponded to the delayed part of an in-beam PET acquisition, i.e. PET acquisition performed right after the end of the irradiation. The paper is organized as follows. Section 2.1 gives details on the electromagnetic and hadronic models used in the GATE simulations. Section 2.2 describes the simulated dual-head PET and OpenPET set-ups. Methods used to assess the sensitivity and

Table 1. Hadronic models used in the GATE simulations. The 'generic ions' correspond to ions heavier than alpha particles.

Hadronic process	Particles	Geant4 processes	Geant4 models	Energy range
Elastic scattering	All particles except low energy neutrons	G4HadronElastic process	G4HadronElastic	0–500 GeV
Elastic scattering	Low energy neutrons	G4HadronElastic process	G4NeutronHPElastic	0–20 MeV
Inelastic process for protons	Protons	G4ProtonInelastic process	G4BinaryCascade	0-500 GeV
Inelastic process for ions	GenericIon, deuteron, triton, ^{3}He, alpha	G4IonInelastic process	G4QMDReaction	0–500 GeV
Inelastic scattering for neutrons	Neutron	G4NeutronInelastic process	G4NeutronHPInelastic	0–20 MeV
			G4BinaryCascade	19 MeV–500 GeV

the spatial resolution are described in sections 2.3 and 2.4 respectively. The realistic clinical head and neck treatment plan simulated in GATE is presented in section 2.5. Results are given in section 3 and discussed in section 4.

2. Material and methods

2.1. GATE simulations

GATE version 6 (Jan *et al* 2011, GATE-Website 2013) is a Monte Carlo simulation application enabling the modeling of emission tomography, transmission tomography and radiation therapy. GATE is based on the Geant4 toolbox. In this work, GATE version 6.2 based on Geant4 version 9.5 was used. As recommended by the Geant4 Electromagnetic Standard working group, the Opt3 electromagnetic standard package parameters were selected. A fine sampling of the cross-section tables (20 bins/decade) was chosen for improved accuracy. Table 1 summarizes the hadronic models used in the head and neck treatment plan simulations to obtain β^+-emitter distributions.

The Geant4 Binary Cascade model (BiC) (Geant4-Website 2013) was applied to protons, ions and neutrons of energies greater than 19 MeV. The high precision neutron package (NeutronHP) was used to transport neutrons down to thermal energies (Geant4-Website 2013). In the case of deuterons, tritons, alpha and ions heavier than alpha particles (so-called 'generic ions'), the G4QMDReactionModel was employed (Koi 2010). This physics list results from the optimization of the Geant4 hadronic models by comparison to PET experimental data. It was already used in Seravalli *et al* (2012) and Robert *et al* (2013), in which the comparison of simulated and experimental data when irradiating a PMMA target with 160 MeV protons showed that GATE overestimated β^+-emitter production rates by about 10% (^{11}C) and 20% (^{15}O). These results, which are considered as sufficient by the community for detector optimization, make the GATE Monte Carlo code appropriate in the context of in-beam PET system optimization.

2.2. Simulated PET configurations

Five realistic clinical PET systems characterized by a 916 mm inner diameter were simulated using GATE. All were composed of 8 rings. Depending on the arrangement, 54 to 72 block-detectors were included in each ring. Each block-detector consisted of 8 (transaxial) $\times$ 8

Table 2. Geometrical parameters of the PET systems simulated with GATE. Except for the number of blocks per ring that decreases with the opening angle for the dual-head PET systems, all parameters were kept identical for all simulations.

FOV	
Diameter (mm)	916
Axial length (mm)	320
Number of rings	8
Blocks	
Number of blocks per ring	72
Axial length (mm)	40
Transaxial length (mm)	40
Crystals	
Number of crystals per block	64
Axial length (mm)	5
Transaxial length (mm)	5
Radial depth (mm)	25
Material	LSO

(axial) array of LSO (Lu_2SiO_5) crystals whose size was $5 \times 5 \times 25$ mm^3 in the transaxial, axial and depth directions. Among the five configurations, two were dual-head PET systems. They were characterized by $\phi = 15^\circ$ and 45° opening angles (figure 1). The highest value $\phi = 45^\circ$ was found to reduce reconstruction artifacts compared to higher opening angles such as $\phi = 100^\circ$ (Crespo *et al* 2006). For the OpenPET configuration, two gaps between the two detector rings ($G = 110$ and 160 mm) were investigated (figure 1). The highest gap value, equal to the axial length of each ring, was chosen to avoid reconstruction artifacts (Yamaya *et al* 2008). The $G = 110$ mm value had an open space close to the $\phi = 15^\circ$ dual-head PET system. A full-ring PET system, without opening, was also simulated as a reference. Table 2 summarizes the geometrical parameters characterizing the full-ring PET system. Except for the number of blocks per ring that decreases with the opening angle for the dual-head PET systems, all parameters were kept identical for all simulations.

In all simulations, the detector response and signal processing were modeled. To mimic a realistic photomultiplier arrangement (4 PMT per block), each block was divided in 4 submodules. Only hits occurring in the same submodule were added by the readout module. The energy resolution was set to 10% at 511 keV and a 420–650 keV energy window was used. 5 ns coincidence windows were used to produce the sinograms.

2.3. Detection sensitivity

A back-to-back point source (1 million pairs of 511 keV gamma particles isotropically emitted) was simulated in air to evaluate the detection sensitivity of each PET system (equation (1)). This point source was either centered in the field-of-view (FOV) or shifted by 229 mm in the transaxial direction or 80 mm in the axial direction to characterize the variability of the sensitivity within the FOV.

$$\text{Sensitivity} = \frac{\text{Number of detected coincidences}}{\text{Number of photon pairs}} \tag{1}$$

2.4. Spatial resolution

Acquisitions of a miniaturized version of the Derenzo phantom (figure 2—left, Derenzo *et al* 1977) including cylindrical inserts between 2 mm to 10 mm in diameter were simulated.

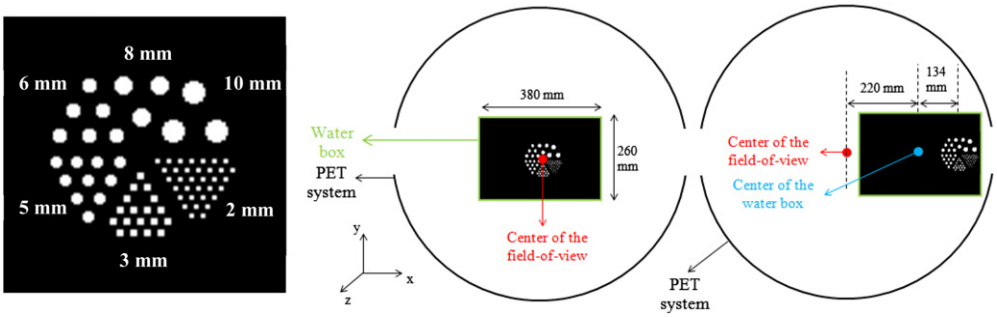

Figure 2. Derenzo phantom (9.2 cm in diameter, 2.4 cm in length) including cylindrical hot inserts of increasing size (2/3/5/6/8/10 mm). The background activity was set to 0 (left). Different positions of the Derenzo phantom and associated water box within the FOV. A dual-head system was illustrated (right). For both locations, the phantom was centered in the axial direction (z-direction) of the PET system.

The active phantom (9.2 cm in diameter, 2.4 cm in length, 10^6 Bq activity) was placed in a large rectangular cuboid scattering medium of respectively 380 (x-axis), 260 (y-axis) and 500 mm (z-axis) dimensions. The scattering medium was entirely made of water and had no background activity. Two positions in the FOV were investigated: the phantom was either placed at the center of the FOV (figure 2—middle) or shifted by 354 mm in the transaxial direction (figure 2—right). For both locations, the phantom was centered in the axial direction. For each configuration, the acquisition duration was adjusted so that 1 million coincidences were detected. A dedicated home-made OS-EM (ordered subset–expectation maximization) reconstruction algorithm (Stute and Comtat 2013) was developed and ten subsets were used. All detected coincidences (trues, scatter and randoms) were included in the reconstruction process. A single-ray Siddon tracing (Siddon 1985) was used to calculate the system matrix. Attenuation was modeled during the reconstruction. The detector response was modeled in the image space as proposed by (Reader *et al* 2002), using a 5 mm FWHM Gaussian function. A 5 mm FWHM Gaussian post-filtering was finally used after reconstruction to decrease noise (Snyder *et al* 1987). The 5 mm FWHM value used in the two Gaussian filters corresponds to the spatial resolution of a clinical PET. The relevance of this value was validated based on the reconstructed images of the Derenzo phantom without any filter in the reconstruction: the 5 mm inserts were the smallest inserts correctly recovered at the center of the FOV. Given the very low counting rates (less than 1% of random coincidences, see results section), no random correction was applied. A single scatter estimation (Barney *et al* 1991) method based on the single scatter sinogram was used to correct for scatter coincidences. For centered and off-centered configurations, $150 \times 150 \times 30$ mm^3 and $940 \times 940 \times 30$ mm^3 volumes were reconstructed respectively. In both cases, the voxel size was $2 \times 2 \times 2$ mm^3.

Curves of the recovery coefficients as a function of the insert diameter (Zito *et al* 1995, Soret *et al* 2007) were plotted for each iteration number of the reconstruction and each PET system. The recovery coefficient was defined as the total activity measured in the true insert contours in the reconstructed images divided by the true activity in the insert.

2.5. Simulations of a small-field head and neck treatment

One field of a realistic proton head and neck treatment plan, originally composed of two fields, was simulated using GATE (figure 3). With this single field, 1 Gy resulting from the irradiation of 870 spots of energies ranging from 102 MeV to 136 MeV was delivered to the planning

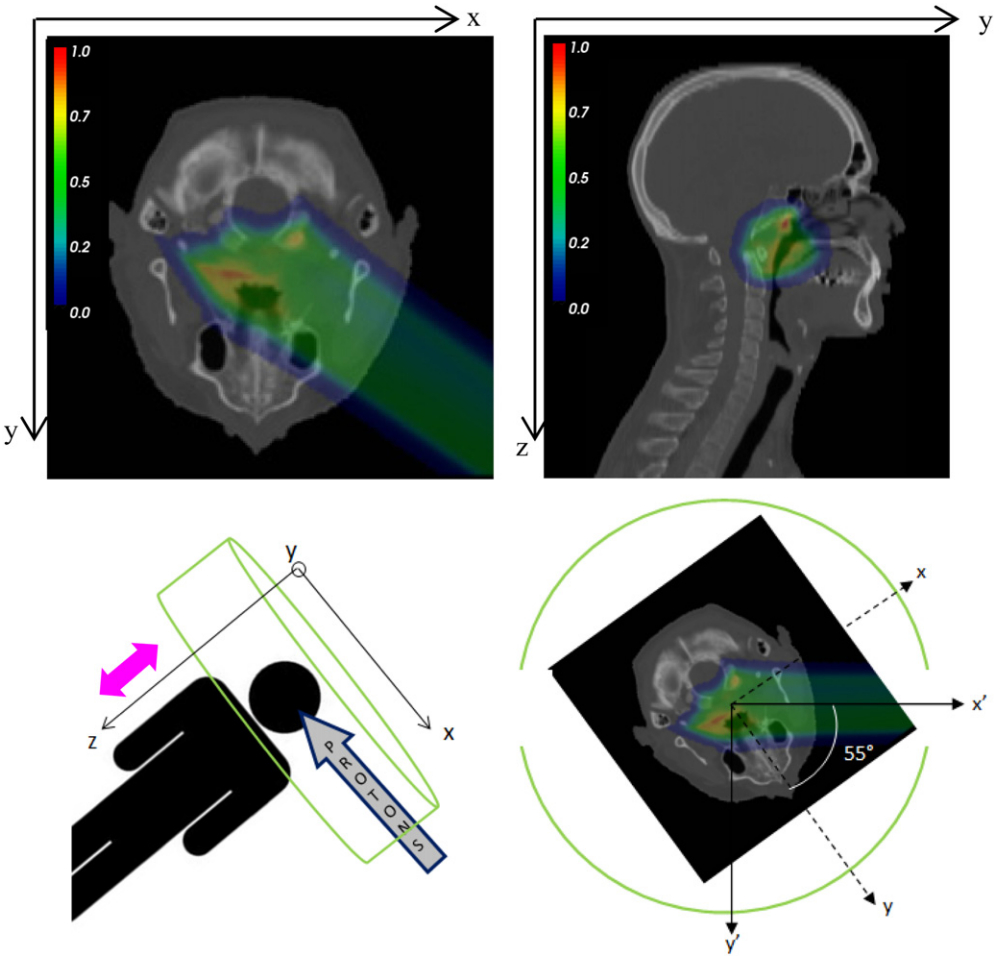

Figure 3. Illustration of the small-field head and neck treatment plan (axial and sagittal planes, top). A total of 2×10^{10} protons were needed to reach the expected 1 Gy dose delivered in the PTV but 1×10^{9} incident protons were actually simulated. The dose was normalized to the maximum. PET system positioning—a dual-head system was illustrated here—in the patient referential (bottom). The pink arrow illustrates displacements of the patient in the z-direction.

target volume (PTV). A total of 1×9 incident protons instead of the 2×10 required to reach the expected dose were simulated for the sake of computation time (about 24 h on 100 CPUs). The β^{+}-emitter distributions (^{11}C, ^{10}C, ^{15}O) were stored. They were then smoothed using a $3 \times 3 \times 3$ mean filter and a 20 scaling factor was applied to obtain the number of particles that would have been emitted for 2×10 incident protons. The resulting maps were used as inputs of the imaging simulations (figure 3). For each system, the acquisition began right after the end of the irradiation and the acquisition duration was set to 300 s. The scenario thus corresponded to the simulation of the delayed part of an in-beam PET acquisition.

Displacements of the patient by 1 and 3 mm were successively introduced in the z (pink arrow, figure 3—inferior/superior displacements) and y-directions (posterior/anterior displacements) to mimic slight mispositionings. To do so, the whole CT map of the patient was moved in the beam referential. To evaluate the ability of each PET system to correctly detect the introduced mispositionings, 25 activity profiles in the y-direction and 25 activity profiles

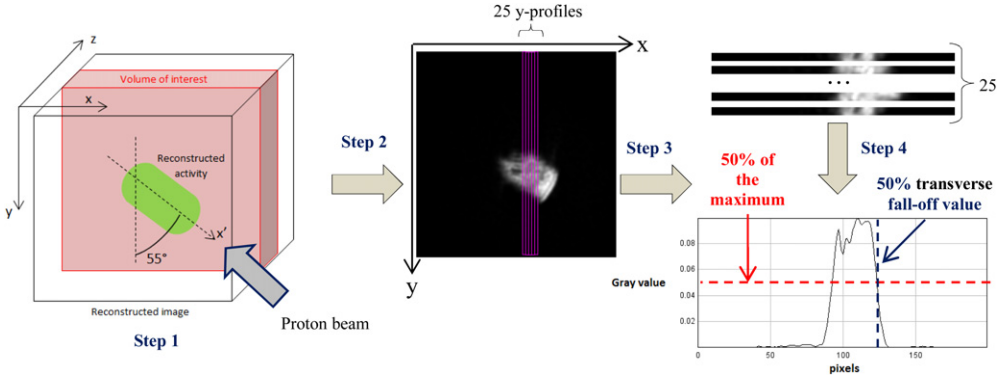

Figure 4. Extraction of the 25 *y*-profiles for the transverse fall-off position estimate.

in the *z*-directions were extracted from the reconstructed images for each configuration and each patient position. The steps required to obtain the 25 profiles in the *y*-direction were as follows (figure 4):

1 Extraction of a 3D volume of interest (200 (*x*-direction) × 200 (*y*-direction) × 5 voxels (*z*-direction)) from the 3D reconstructed images of 200 × 200 × 200 voxels,
2 Summation of the resulting 3D volume of interest along the *z*-direction, so as to get a 2D 200 × 200 voxel image in a (*xy*) plane.
3 Extraction of 25 *y*-profiles (200 voxels) from the 2D 200 × 200 voxel image obtained at step 2,
4 Measurement of the transverse fall-off distance (30% and 50% of the maximum value were investigated) on each profile.

A similar procedure was used to extract the 25 *z*-profiles from the 3D reconstructed images. For each PET system *i*, mispositionings of the patient were estimated by subtracting the transverse fall-off distances measured from the 25 *y* and *z*-activity profiles obtained for two different positionings of the patient. For instance, equation (2) gives the calculation of the estimated mispositioning when a 3 mm displacement was introduced in the *y*-direction (0–3 mm *y*-shift). The corresponding uncertainty σ was deduced by calculating the standard deviation of the 25 transverse fall-off value differences (equation (3)). In total, four mispositionings were studied: two 1 mm displacements (0–1 mm shift in the *y*- and *z*-directions) and two 3 mm displacements (0–3 mm shift in the *y*- and *z*-directions). The estimated mispositionnings were then compared to the real shifts introduced in the simulations to define the error ε.

$$\text{Estimated shift}_{i,0-y3\text{ mm}} = \frac{\sum_{25\ y-\text{profiles}} (\text{fall off value}_{y3\text{ mm}} - \text{fall off value}_{0\text{ mm}})}{25} \tag{2}$$

$$\sigma^2_{i,0-y3\text{ mm}} = \frac{\sum_{25\ y-\text{profiles}} (\text{fall off value}_{y3\text{ mm}} - \text{fall off value}_{0\text{ mm}})^2}{25} - (\text{Estimated shift}_{i,0-y3\text{ mm}})^2. \tag{3}$$

In previous studies (Parodi *et al* 2002, 2007c), the β^+-emitter maps obtained from Monte Carlo simulations were convolved using a 3D Gaussian kernel to bypass the complete modeling of the imaging and reconstruction processes. To determine whether this simplification could yield erroneous estimates of the patient mispositioning, we convolved the simulated β^+-emitter maps resulting from the treatment simulations by a 5 mm FWHM 3D Gaussian kernel

Table 3. Detection sensitivity values for the two dual-head systems and two OpenPET configurations. Values corresponding to the full-ring PET system are also given. Sensitivities were calculated in the center of the FOV and at two off-centered positions.

		Dual-head		OpenPET	
	Full-ring PET	$\phi = 15^\circ$	$\phi = 45^\circ$	$G = 110$ mm	$G = 160$ mm
Center	7.0%	6.4%	5.2%	6.6%	6.4%
Transaxial shift	6.2%	5.5%	4.0%	3.9%	2.9%
Axial shift	3.6%	3.3%	2.7%	1.2%	0.2%

Table 4. Percentages of true, single scatter, multiple scatter and random coincidences obtained for the different Derenzo acquisitions.

			Dual-head		OpenPET	
		Full-ring PET	$\phi = 15^\circ$	$\phi = 45^\circ$	$G = 110$ mm	$G = 160$ mm
Center	Trues	55.8	55.7	56.8	62.7	65.4
	Single Scatters	33.4	32.6	31.5	28.5	26.6
	Multiple Scatters	13.1	12.6	11.3	12.4	11.9
	Randoms	0.4	0.5	0.5	0.5	0.5
Trans-axial shift	Trues	52.0	53.3	55.4	48.2	47.4
	Singles Scatters	35.8	35.1	33.7	37.1	37.2
	Multiple Scatters	11.7	11.2	10.5	13.8	14.3
	Randoms	0.4	0.5	0.4	0.9	1.0

(estimated FWHM in the reconstructed PET image). The difference between the transverse fall-off positions observed in the images obtained with the different PET systems (reconstructed images after complete modeling of the imaging) and the transverse fall-off positions observed in the convolved images (no modeling of the imaging and no reconstruction) was then calculated in the configuration in which the patient was accurately positioned. Non-zero differences would suggest that a full modeling of the imaging and reconstruction processes is required to correctly evaluate patient mispositionings (Jan *et al* 2013).

3. Results

3.1. Detection sensitivity

Table 3 compares the detection sensitivity values obtained with the full-ring, dual-head and OpenPET systems. Although the sensitivity is similar at the center of the FOV for all systems, it is far more uniform across the FOV for the dual-head systems than for the OpenPET systems.

3.2. Spatial resolution

Table 4 shows the percentages of each coincidence type (trues, single scatter, multiple scatter and randoms) for the different Derenzo acquisitions. As expected, random coincidences are negligible (less than 1%) but scatter clearly needs to be corrected. Curves of the recovery coefficients as a function of the insert diameter were plotted for each PET configuration for different numbers of iterations in the reconstruction process (5, 10, 20, 30 and 50). We found that the convergence in terms of recovery coefficient was achieved for each insert size from 20 iterations (results not shown). Recovery coefficients corresponding to the full-ring PET, dual-head PET systems ($\phi = 15$ and 45°) and OpenPET systems ($G = 110$ and 160 mm)

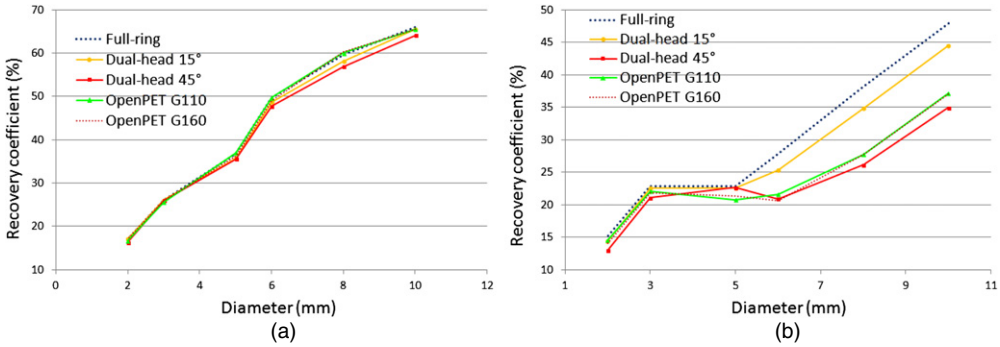

Figure 5. Recovery coefficients as a function of the insert diameter obtained for each PET system (20 iterations). The Derenzo phantom was either placed at the center of the FOV (a) or transaxially off-centered by 35.4 cm (b).

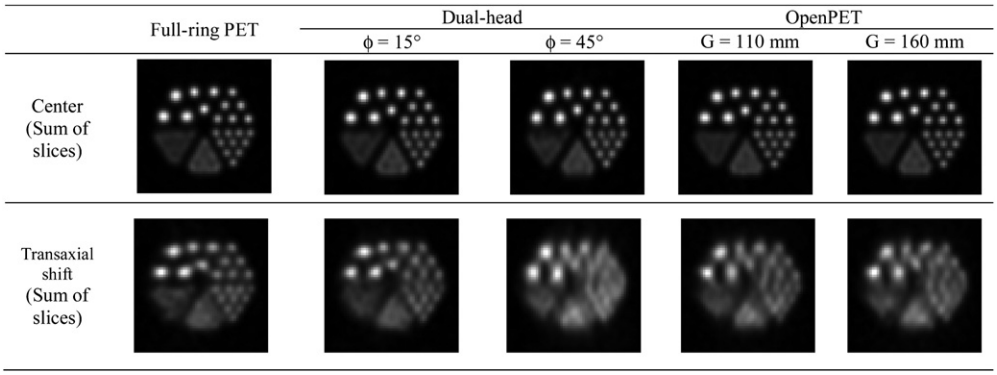

Figure 6. Reconstructed images of the Derenzo phantom (20 iterations). The Derenzo phantom was either placed at the center of the FOV or transaxially off-centered by 35.4 cm.

are plotted in figure 5 for 20 iterations. Figure 6 illustrates the Derenzo phantom images obtained with the different PET systems for 20 iterations. Figures 5 and 6 suggest that the spatial resolution strongly depends on the location of the phantom within the FOV for all PET scanner geometries. This dependence is higher for the $\phi = 45^\circ$ dual-head system and for the two OpenPET systems. For these three systems, the recovery coefficient corresponding to the 10 mm inserts respectively decreased by 45.5%, 43.4% and 43.6% compared to the values obtained when the Derenzo phantom was at the center of the FOV.

3.3. Realistic simulations of a head and neck treatment

Figure 7 illustrates slices of the 3D β^+-emitter maps directly obtained using GATE (no imaging and reconstruction steps) when the patient was shifted by 3 mm in the *y*-direction. The slices shown in figures 7(b) and 7(c) correspond to the ^{11}C and ^{15}O β^+-emitters respectively. The corresponding CT-slice of the patient and dose distribution are shown (figure 7(c)). As expected, a good correlation was observed between ^{11}C stopping positions and bone and fatty structures as well as between ^{15}O and soft tissues. The numbers of β^+-emitters produced during the realistic irradiation and the numbers of detected coincidences (no shift configuration) are given in tables 5 and 6. Among the dedicated systems, the $\phi = 15^\circ$ dual-head system had the highest sensitivity (1.06%). The $\phi = 45^\circ$ dual-head system, $G = 110$ mm and $G = 160$ mm

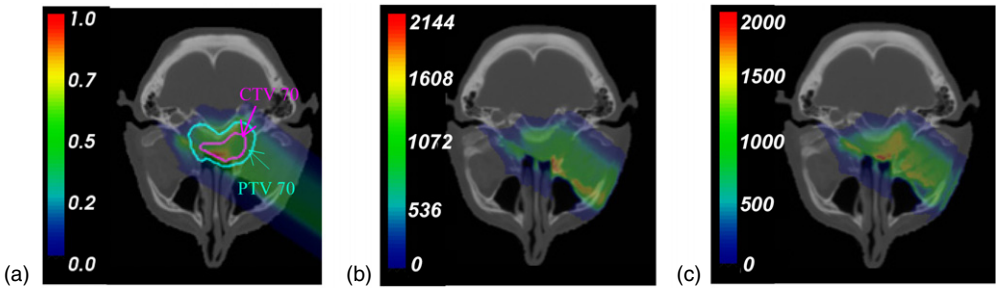

Figure 7. Slices through the 3D dose distribution and the 3D β^+-emitter maps obtained by simulating a realistic head and neck treatment plan in GATE, superimposed onto the patient's CT: (a) dose distribution, (b) ^{11}C, (c) ^{15}O. In figure (a), the corresponding PTV 70 (planning target volume–70 Gy) and CTV 70 (clinical target volume–70 Gy) contours are also shown. The dose distribution and numbers of β^+-emitters are shown in rainbow colors.

Table 5. Total numbers of β^+-emitters (^{11}C, ^{10}C, ^{15}O) produced during the GATE head and neck treatment plan simulation (no shift configuration, 2×10^{10} incident protons).

	Numbers of β^+-emitters produced during the simulated head and neck irradiation
^{11}C	2.76×10^8
^{10}C	2.54×10^7
^{15}O	2.57×10^8

Table 6. Numbers of coincidences detected by the PET systems (no shift configuration).

		Dual-head		OpenPET	
	Full-ring PET	$\phi = 15^\circ$	$\phi = 45^\circ$	$G = 110$ mm	$G = 160$ mm
Number of coincidences	3.42×10^6	2.98×10^6	2.46×10^6	2.60×10^6	2.42×10^6
Sensitivity (%)	1.23	1.06	0.88	0.93	0.87

OpenPET systems had 21%, 14% and 23% lower sensitivities compared to the $\phi = 15^\circ$ dual-head system.

Figure 8 shows a reconstructed β^+-emitter slice obtained with the full-ring and two dedicated PET systems ($\phi = 15^\circ$ dual-head system and $G = 110$ mm OpenPET system) when the patient was correctly positioned. The reconstructed maps corresponded to 20 iterations. The corresponding slice used as an input of the imaging simulations and the expected reconstructed map, obtained by convolving the input β^+-emitter distribution by a 3D 5 mm-FWHM Gaussian kernel, are shown in figure 9. In both figures, profiles of the activity along two directions (x', which made a 55° angle with the patient's x-axis—figure 4—and the orthogonal direction y') are plotted to quantitatively compare the images.

Figure 10 shows the mean z-profiles obtained from each β^+-emitter map used as input for the imaging simulations. Three configurations were analyzed: 0, 1 and 3 mm z-shifts. Only disintegrated β^+-emitters were considered. The mean z-profiles were deduced by averaging the 25 z-profiles. Table 7 summarizes the shift values deduced from figure 10 and the corresponding values for the y-shifts. Either the 30% or the 50% of the maximum value were used to determine the transverse fall-off positions. Results were in good agreement with the shifts introduced in the simulations with errors ε less than 10% for y and z-shifts when the 30% transverse fall-off value was used.

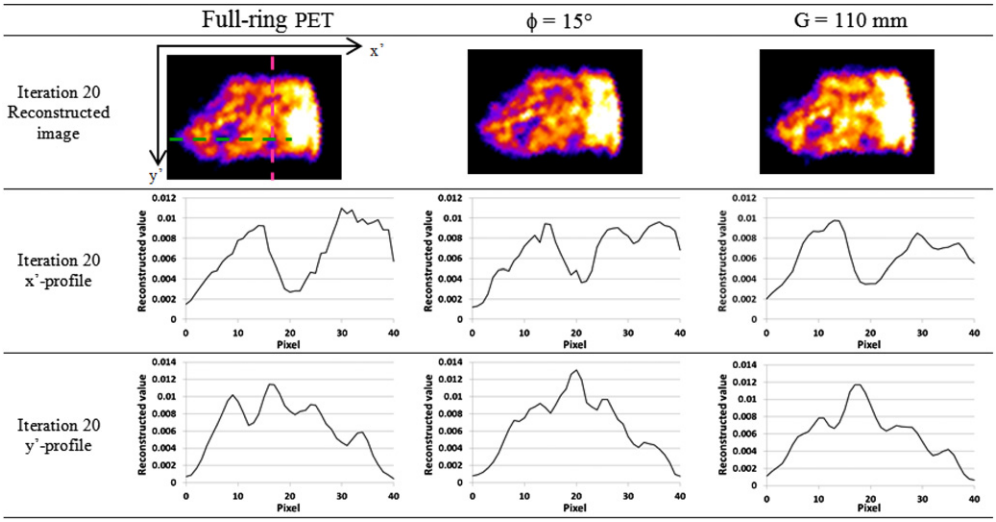

Figure 8. First row: slices of the reconstructed 3D β^+-emitter (20 iterations OS-EM) maps for 3 PET systems (full-ring, $\phi = 15^\circ$ dual-head system and $G = 110$ mm OpenPET system). The second and third rows show x'- (green line) and y'-profiles (pink line) deduced from the reconstructed images.

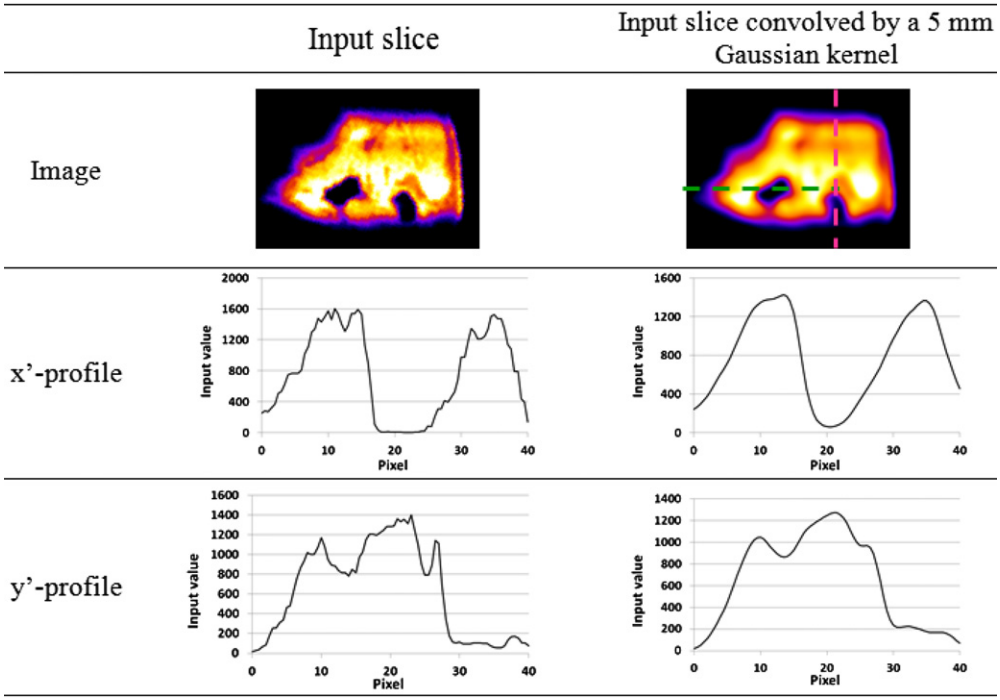

Figure 9. Slice of the 3D β^+-emitter map used as an input of the imaging simulation (first column). Slice of the map obtained by convolving the input β^+-emitter distribution by a 3D 5 mm-FWHM Gaussian kernel (second column). The second and third rows show x'- (green line) and y'-profiles (pink line) deduced from the input slices.

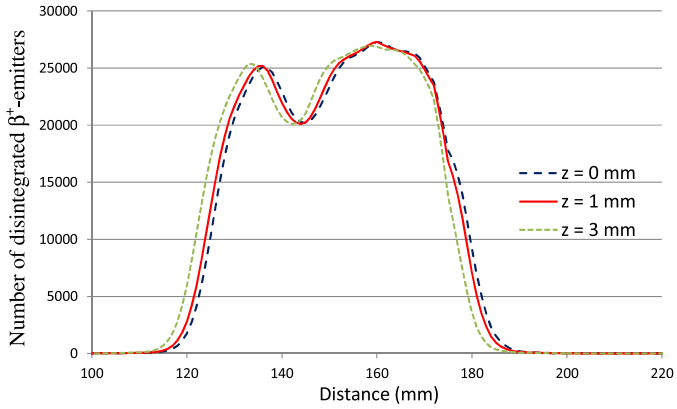

Figure 10. Mean z-profiles of the summed images obtained from the β^+-emitter maps used as inputs of the imaging simulations for z-shifts of 0, 1 and 3 mm. Only the ^{11}C, ^{10}C and ^{15}O disintegrated during the PET acquisition were considered.

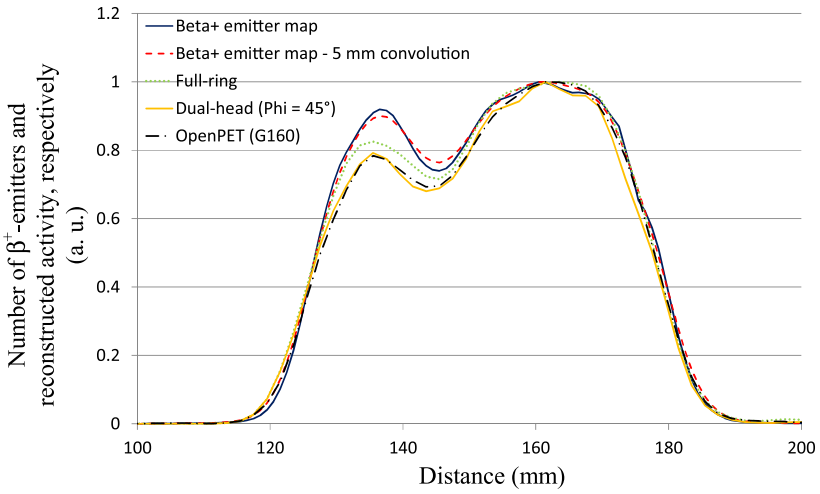

Figure 11. Mean z-profiles plotted on the summed images obtained from the input (blue solid and red dashed lines) and reconstructed activity maps (green dotted, yellow solid and black dash–dotted lines). No shift was introduced in the treatment simulation.

Table 7. Shift values (equation (2)) determined from y and z-profiles plotted on the summed images obtained from the input β^+-emitter maps for two transverse fall-off distance definitions: 30% and 50% of the maximum value.

	y-shifts		z-shifts	
	0–1 mm shift	0–3 mm shift	0–1 mm shift	0–3 mm shift
30% of the maximum	1.1 ± 0.6	3.3 ± 0.8	0.9 ± 0.2	3.1 ± 1.0
50% of the maximum	0.9 ± 0.5	3.0 ± 1.5	0.9 ± 0.7	2.6 ± 1.1

Figure 11 shows the mean z-profiles obtained with the full-ring and two dedicated PET ($\phi = 45^\circ$ and G = 160°) systems when no shift was introduced in the simulations. Profiles obtained by convolving the β^+-emitter input maps by a 3D Gaussian kernel (5 mm FWHM)

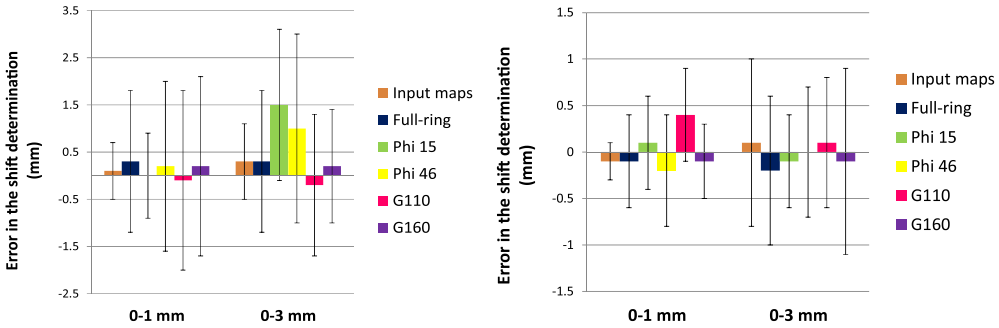

Figure 12. Errors (ε) in the shift estimates (mm) for the different PET systems. The patient was moved in the y-direction (30% transverse fall-off value, left) and in the z-direction (30% transverse fall-off value, right). 'Input maps' errors were deduced by comparing the shifts estimated using the simulated β^+-emitter maps (inputs of the imaging simulations) to the actual shifts introduced in the simulations.

Table 8. z-shifts (equation (2)) estimated from the reconstructed PET images, for two definitions of the transverse fall-off distance and five PET systems.

	0–1 mm shift		0–3 mm shift	
	30%	50%	30%	50%
Full-ring PET	0.9 ± 0.5	1.0 ± 0.8	2.8 ± 0.8	2.6 ± 1.1
$\phi = 15°$	1.1 ± 0.5	0.6 ± 0.4	2.9 ± 0.5	2.4 ± 0.7
$\phi = 45°$	0.8 ± 0.6	0.7 ± 0.8	3.0 ± 0.7	2.3 ± 1.0
$G = 110$ mm	1.4 ± 0.5	1.2 ± 0.8	3.1 ± 0.7	2.8 ± 0.8
$G = 160$ mm	0.9 ± 0.4	0.7 ± 0.4	2.9 ± 1.0	2.6 ± 0.8

Table 9. y-shifts (equation (2)) estimated from the reconstructed PET images, for two definitions of the transverse fall-off distance and five PET systems.

	0–1 mm shift		0–3 mm shift	
	30%	50%	30%	50%
Full-ring PET	1.3 ± 1.5	1.0 ± 1.5	3.3 ± 1.5	3.7 ± 2.2
$\phi = 15°$	1.0 ± 0.9	1.0 ± 3.0	4.5 ± 1.6	3.7 ± 3.7
$\phi = 45°$	1.2 ± 1.8	2.2 ± 2.7	4.0 ± 2.0	4.5 ± 3.1
$G = 110$ mm	0.9 ± 1.9	1.1 ± 2.3	2.8 ± 1.5	3.6 ± 2.5
$G = 160$ mm	1.2 ± 1.9	1.9 ± 1.7	3.2 ± 1.2	3.7 ± 1.9

are also plotted. All dedicated systems correctly reproduced the profiles obtained with the full-ring PET.

Shift values determined from the z-profiles plotted in figure 11 and similar profiles obtained when the patient was z or y-shifted are given in tables 8 and 9. Except for the $\phi = 15°$dual-head system, the estimated shifts, compared to the shifts introduced in the simulations, had errors ε less than or equal to 1 mm for all PET systems (figure 12).

Table 10 shows mean y and z-differences determined between the 50% transverse fall-off distances observed in the images obtained with the different PET systems and the transverse fall-off distance observed in the convolved image when the patient is well-positioned. The values should be equal to 0 mm if the convolution step was sufficient to bypass the modeling of the imaging and reconstruction processes.

Table 10. Mean y and z-differences between the transverse fall-off distances (50% transverse fall-off value) observed in the images obtained with the different PET systems and the transverse fall-off distance observed in the convolved image when the patient is well-positioned.

	Full-ring PET	$\phi = 15^\circ$	$\phi = 45^\circ$	$G = 110$ mm	$G = 160$ mm
y-Difference (mm)	-1.2 ± 1.2	-0.8 ± 1.1	1.9 ± 2.5	-1.2 ± 0.6	-1.2 ± 1.3
z-Difference (mm)	1.0 ± 0.6	1.4 ± 0.8	1.5 ± 0.7	0.7 ± 0.5	1.0 ± 0.4

4. Discussion

In this work, dual-head and OpenPET systems have been modeled for the first time in GATE. Identical simulation parameters have been used to objectively compare the two systems. The detector electronics has been realistically modeled.

The detection sensitivity of each system has been first estimated using a point source located at different positions within the FOV. For equivalent opening angles ($\phi = 15^\circ$ and $G = 110$ mm), the dual-head systems had 41% and 168% higher detection efficiencies than the OpenPET systems in the transaxial and axial directions respectively (table 3). This feature is of crucial importance for PET-based dose delivery verification in hadrontherapy given the low production yields of annihilation photons (Parodi *et al* 2005, Crespo *et al* 2006).

Using a Derenzo phantom, the spatial resolutions achievable by the two systems have then been characterized, using curves of the recovery coefficients as a function of the insert diameter (figure 5) for two locations of the phantom within the FOV. Results showed that the spatial resolution strongly depends on the location of the phantom within the FOV especially for the $\phi = 45^\circ$ dual-head system and for the two OpenPET systems. For the $\phi = 45^\circ$ dual-head PET system, reconstruction artifacts due to the incomplete angular sampling (elongation of the imaged objects in the y-direction) as already observed in Crespo *et al* (2006) are clearly visible (figure 6).

Realistic simulations of a small-field head and neck treatment plan have been performed. Several configurations corresponding to 1 and 3 mm patient mispositionings have been studied. Production yields of 1.4×10^{-2} (^{11}C), 1.3×10^{-3} (^{10}C) and 1.3×10^{-2} (^{15}O) per incident proton have been obtained by integrating the GATE β^+-emitter production maps (table 5). These values are consistent with experimental production rates reported by (Parodi 2004) as well as with the integral production yields of β^+-emitters evaluated by simulating a 1 Gy head and neck treatment plan in FLUKA (Parodi *et al* 2008). Activity profiles drawn from the reconstructed PET images showed that all investigated systems could reproduce almost identically the profiles obtained for a full-ring PET system. Transverse fall-off distances have been calculated to assess the ability of the PET systems to correctly evaluate patient mispositionings introduced in the simulations. For all systems, errors in the estimates of the patient shift and associated uncertainties were always less than 2 mm (figure 12). These results are extremely encouraging given that a millimetric accuracy is targeted.

These conclusions were obtained for a head and neck treatment plan characterized by a small and centered imaged volume. They should however not be extended to all clinical cases. A large field prostate treatment plan was also simulated (figure 13). In this case, the OpenPET systems reproduced almost identically the profiles obtained for a full-ring PET system, but significant differences in shape were observed for dual-head systems. These differences can be explained by the reconstruction artifacts due to incomplete angular sampling that tend to elongate the imaged objects at the edges of the FOV. For the $\phi = 45^\circ$ dual-head PET system, the observed artifacts led to significant errors, up to 4 mm, in the patient shift estimate (figure 13).

In most papers related to PET-based dose delivery verification in hadrontherapy, no modeling of the actual PET imaging process and associated reconstruction was included. In

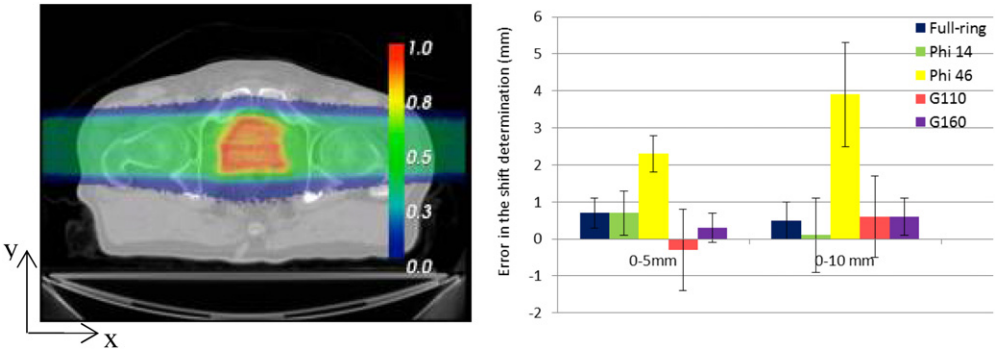

Figure 13. Illustration of the large field prostate treatment plan (transverse plane, left). Errors (ε) in the shift estimates (mm) for the different PET systems. The patient was moved in the y-direction (50% transverse fall-off value, right).

Table 11. Pros and cons of the different simulated PET geometries for the monitoring of the delivered dose in protontherapy.

		Detection sensitivity	Spatial resolution	Ability to estimate patient mispositioning (Small-field treatment plan)	Ability to estimate patient mispositioning (Large field treatment plan)
Dual-head systems	$\phi = 15^\circ$	++	++	+	+
	$\phi = 45^\circ$	+	−	−	−
OpenPET systems	$G = 110$ mm	−	−	+	+
	$G = 160$ mm	−	−	+	+

Parodi *et al* (2002) and Parodi *et al* (2007c), the simulated β^+-emitter production maps were convolved by 3D-Gaussian kernel to mimic the detector response. This Gaussian smoothing was adjusted based on the comparison of measured and simulated data for phantom experiments. This practical approach, which did not require access to confidential scanner information, was only applied to full-ring architectures. Figure 11 compares profiles obtained with and without modeling of the imaging and reconstruction processes. For this head and neck treatment case, the figure suggests that the imaging and reconstruction process modeling had little added-value compared to a simple convolution of the β^+-emitter production maps by a 3D-Gaussian kernel. This observation was mitigated by table 10: differences between the transverse fall-off distances observed in the images obtained with the different PET systems and the transverse fall-off distance observed in the convolved image without any displacement were up to 1.9 mm for the $\phi = 45^\circ$ dual-head system. These differences, observed on a small volume centered in the FOV, might increase for larger volumes (Jan *et al* 2013). For all systems, the hypothesis of a stationary Gaussian blurring is insufficient to get the millimetric precision required in hadrontherapy. For dual-head systems, the modeling of the detector response and reconstruction process is also required to reproduce reconstruction artifacts resulting from the incomplete angular sampling.

Table 11 summarizes the pros and cons of the different systems. It suggests that dual-head systems characterized by small opening angles might be preferred to OpenPET geometries.

To compare the performances of the dedicated PET systems, realistic but arbitrary crystal dimensions and PMT arrangements have been chosen. These choices impact the Point Spread Function of the systems and thus the transverse fall-off regions of the reconstructed images that were compared in the head and neck treatment simulations. The reported values (tables 8–10)

might vary depending on the detector intrinsic characteristics, although the trends between detector geometries are expected to remain unchanged.

In our study, the system matrix used for image reconstruction only modeled the detector geometry and used single-ray Siddon tracing to estimate the contribution of a voxel to a line of response. The per-iteration convolution was set identically for all imaging systems. The difference in spatial resolution performance between systems might thus be reduced by further optimization of the system matrix for each scanner.

In this work, in-beam PET acquisitions have been investigated but no wash-out modeling was taken into account. Our next investigations will include studying the impact of the counting statistics (i.e. acquisition duration, duration between the end of the treatment and the beginning of the PET acquisition) on the accuracy of the patient mispositioning estimates, and introduction of a biological wash-out model in the simulations.

Only one dimensional patient mispositionings have been considered in this study. More complex cases including 2D patient mispositioning and/or modification of the patient CT to mimic anatomical modifications between the time the treatment plan is established and the treatment session itself should also be investigated, as well as alternative PET architectures (Crespo *et al* 2007, Yamaya *et al* 2008, 2009).

5. Conclusions

OpenPET and dual-head dedicated PET systems have been simulated and compared in terms of sensitivity, spatial resolution and ability to evaluate patient mispositionings introduced in the simulations. The dual-head systems yield more uniform detection sensitivity within the FOV than the OpenPET systems. The spatial resolution strongly depended on the location within the FOV for the $\phi = 45^\circ$ dual-head system and for the two OpenPET systems. For the simulated small-field head and neck treatment, all simulated systems could estimate the introduced mispositionings of the patient with a millimetric accuracy.

References

Adam L E, Karp J S and Brix G 1999 Investigation of scattered radiation in 3D whole-body positron emission tomography using Monte Carlo simulations *Phys. Med. Biol.* **44** 2879–95

Agostinelli S, Allison J, Amako K, Apostolakis J and Araujo H 2003 Geant4-a simulation toolkit *Nucl. Instrum. Methods Phys. Res.* A **506** 250–303

Barney J S, Rogers J G, Harrop R and Hoverath H 1991 Object shape dependent scatter simulations for PET *IEEE Trans. Nucl. Sci.* **38** 719–25

Battistoni G *et al* 2007 The FLUKA code: description and benchmarking *AIP Conf. Proc. Proc. Hadronic Shower Simulation Workshop (Fermilab 6–8 Sept. 2006* vol 896*)* ed M Albrow and R Raja pp 31–49

Crespo P, Shakirin G and Enghardt W 2006 On the detector arrangement for in-beam PET for hadron therapy monitoring *Phys. Med. Biol.* **51** 2143–63

Crespo P, Shakirin G, Fiedler F, Enghardt W and Wagner A 2007 Direct time-of-flight for quantitative, real-time in-beam PET: a concept and feasibility study *Phys. Med. Biol.* **52** 6795–811

Derenzo S E, Budinger T F, Cahoon J L, Huesman R H and Jackson H G 1977 High resolution computed tomography of positron emitters *IEEE Trans. Nucl. Sci.* **24** 544–58

Enghardt W, Crespo P, Fiedler F, Hinz R, Parodi K, Pawelke J and Pönisch F 2004 Charged hadron tumour therapy monitoring by means of PET *Nucl. Instrum. Methods Phys. Res.* A **525** 284–8

Enghardt W, Debus J, Haberer T, Hasch B G, Hinz R, Jäkel O, Krämer M, Lauckner K, Pawelke J and Pönisch F 1999 Positron emission tomography for quality assurance of cancer therapy with light ion beams *Nucl. Phys.* A **654** 1047c–50c

Fiedler F, Priegnitz M, Jülich R, Pawelke J, Crespo P, Parodi K, Pönisch F and Enghardt W 2008 In-beam PET measurements of biological half-lives of 12C irradiation induced β^+-activity *Acta Oncol.* **47** 1077–86

GATE-Website 2013 www.opengatecollaboration.org

Geant4-Website 2013 http://geant4.web.cern.ch/geant4/UserDocumentation/UsersGuides/PhysicsReference Manual/BackupVersions/V9.5/fo/PhysicsReferenceManual.pdf

Iseki Y *et al* 2003 Positron camera for range verification of heavy-ion radiotherapy *Nucl. Instrum. Methods Phys. Res.* A **515** 840–9

Jan S, Frisson T and Sarrut D 2013 GATE simulation of 12C hadrontherapy treatment combined with a PET imaging system for dose monitoring: a feasibility study *IEEE Trans. Nucl. Sci.* **60** 423–9

Jan S *et al* 2004 GATE: a simulation toolkit for PET and SPECT *Phys. Med. Biol.* **49** 4543–61

Jan S *et al* 2011 GATE V6: a major enhancement of the GATE simulation platform enabling modelling of CT and radiotherapy *Phys. Med. Biol.* **56** 881–901

Koi T 2010 New native QMD code in Geant4 *MC2010: Joint Int. Conf. on Supercomputing in Nuclear Applications and Monte Carlo (Tokyo, Japan, 17–21 Oct.)* http://geant4.cern.ch/results/papers/QMD-MC2010.pdf

Llacer J 1988 Positron emission medical measurements with accelerated radioactive ion beams *Nucl. Sci. Appl.* **3** 111–31

Nishio T, Miyatake A, Ogino T, Nakagawa K, Saijo N and Esumi H 2010 The development and clinical use of a beam on-line PET system mounted on a rotating gantry port in proton therapy *Int. J. Radiat. Oncol. Biol. Phys.* **76** 277–86

Parodi K 2004 On the feasibility of dose quantification with in-beam PET data in radiotherapy with ^{12}C and proton beams *PhD Thesis* Technische Universität Dresden, Dresden, Germany

Parodi K, Bortfeld T and Haberer T 2008 Comparison between in-beam and offline positron emission tomography imaging of proton and carbon ion therapeutic irradiation at synchrotron and cyclotron-based facilities *Int. J. Radiat. Oncol. Biol. Phys.* **71** 945–56

Parodi K, Enghardt W and Haberer T 2002 In-beam PET measurements of β^+ radioactivity induced by proton beams *Phys. Med. Biol.* **47** 21–36

Parodi K, Ferrari A, Sommerer F and Paganetti H 2007c Clinical CT-based calculations of dose and positron emitter distributions in proton therapy using the FLUKA Monte Carlo code *Phys. Med. Biol.* **52** 3369–87

Parodi K, Paganetti H, Cascio E, Flanz J, Bonab A, Alpert N, Lohmann K and Bortfeld T 2007b PET/CT imaging for treatment verification after proton therapy—a study with plastic phantoms and metallic implants *Med. Phys.* **34** 419–35

Parodi K, Pönisch F and Enghardt W 2005 Experimental study on the feasibility of in-beam PET for accurate monitoring of proton therapy *IEEE Trans. Nucl. Sci.* **52** 778–86

Parodi K *et al* 2007a Patient study on *in vivo* verification of beam delivery and range, using positron emission tomography and computed tomography imaging after proton therapy *Int. J. Radiat. Oncol. Biol. Phys.* **68** 920–34

Pawelke J, Enghardt W, Haberer T, Hasch B G, Hinz R, Kramer M, Lauckner E and Sobiella M 1997 In-beam PET imaging of the control of heavy-ion tumour therapy *IEEE Trans. Nucl. Sci.* **44** 1492–8

Pönisch F, Parodi K, Hasch B G and Enghardt W 2004 The modelling of positron emitter production and PET imaging during carbon ion therapy *Phys. Med. Biol.* **49** 5217–32

Pshenichnov I, Mishustin I and Greiner W 2006 Distributions of positron-emitting nuclei in proton and carbon-ion therapy studied with Geant4 *Phys. Med. Biol.* **51** 6099–112

Reader A J, Ally S, Bakatselos F, Manavaki R, Walledge R J, Jeavons A P, Julyan P J, Zhao S, Hastings D L and Zweit J 2002 One-pass list-mode EM algorithm for high-resolution 3-D PET image reconstruction into large arrays *IEEE Trans. Nucl. Sci.* **49** 693–9

Robert C *et al* 2013 Distributions of secondary particles in proton and carbon-ion therapy: a comparison between GATE/Geant4 and FLUKA Monte Carlo codes *Phys. Med. Biol.* **58** 2879–99

Seravalli E *et al* 2012 Monte Carlo calculations of positron emitter yields in proton radiotherapy *Phys. Med. Biol.* **57** 1659–73

Shakirin G, Braess H, Fiedler F, Kunath D, Laube K, Parodi K, Priegnitz M and Enghardt W 2011 Implementation and workflow for PET monitoring of therapeutic ion irradiation: a comparison of in-beam, in-room and off-line techniques *Phys. Med. Biol.* **56** 1281–98

Siddon R 1985 Fast calculation of the exact radiological path for a three-dimensional CT array *Med. Phys.* **12** 252–5

Snyder D L, Miller M I, Thomas L J and Politte D G 1987 Noise and edge artifacts in maximum-likelihood reconstructions for emission tomography *IEEE Trans. Med. Imaging* **6** 228–38

Sommerer F, Cerutti F, Parodi K, Ferrari A, Enghardt W and Aiginger H 2009 In-beam PET monitoring of mono-energetic ^{16}O and ^{12}C beams: experiments and FLUKA simulations for homogeneous targets *Phys. Med. Biol.* **54** 3979–96

Sommerer F, Parodi K, Ferrari A, Poljanc K, Enghardt W and Aiginger H 2006 Investigating the accuracy of the FLUKA code for transport of therapeutic ion beams in matter *Phys. Med. Biol.* **51** 4385–98

Soret M, Bacharach S L and Buvat I 2007 Partial-volume effect in PET tumor imaging *J. Nucl. Med.* **48** 932–945

Stute S and Comtat C 2013 Practical considerations for image-based PSF and blobs reconstruction in PET *Phys. Med. Biol.* **58** 3849–70

Surti S, Karp J S and Muehllehner G 2004 Image quality assessment of LaBr3-based whole-body 3D PET scanners: a Monte Carlo evaluation *Phys. Med. Biol.* **49** 4593–610

Surti S, Zou W, Daube-Witherspoon M E, McDonough J and Karp J S 2011 Design study of an *in situ* PET scanner for use in proton beam therapy *Phys. Med. Biol.* **56** 2667–85

Tashima H, Yamaya T, Yoshida E, Kinouchi S, Watanabe M and Tanaka E 2012 A single-ring OpenPET enabling PET imaging during radiotherapy *Phys. Med. Biol.* **57** 4705–18

Titt U, Bednarz B and Paganetti H 2012 Comparison of MCNPX and Geant4 proton energy deposition predictions for clinical use *Phys. Med. Biol.* **57** 6381–93

Yamaya T, Inaniwa T, Minohara S, Yoshida E, Inadama N, Nishikido F, Shibuya K, Fung Lam C and Murayama H 2008 A proposal of an open PET geometry *Phys. Med. Biol.* **53** 757–73

Yamaya T, Inaniwa T, Yoshida E, Nishikido F, Shibuya K, Inadama N and Murayama H 2009 Simulation studies of a new 'OpenPET' geometry based on a quad unit of detector rings *Phys. Med. Biol.* **54** 1223–33

Yoshida E, Kinouchi S, Tashima H, Nishikido F, Inadama N, Murayama H and Yamaya T 2012 System design of a small OpenPET prototype with 4-layer DOI detectors *Radiol. Phys. Technol.* **5** 92–97

Zhu X, Espana S, Daartz J, Liebsch N, Ouyang J, Paganetti H, Bortfeld T R and El Fakhri G 2011 Monitoring proton radiation therapy with in-room PET imaging *Phys. Med. Biol.* **56** 4041–57

Zito F, Gilardi M C, Magnani P and Fazio F 1995 Single-photon emission tomographic quantification in spherical objects: effects of object size and background *Eur. J. Nucl. Med.* **23** 263–71